



HAL
open science

Physical Interactions Tune the Chemisorption of Polar Anions on Carbon Nanostructures

Anwar Hasmy, Luis Rincón, Adrien Noury, François Henn, Vincent Jourdain

► **To cite this version:**

Anwar Hasmy, Luis Rincón, Adrien Noury, François Henn, Vincent Jourdain. Physical Interactions Tune the Chemisorption of Polar Anions on Carbon Nanostructures. *Journal of Physical Chemistry C*, 2022, 126 (31), pp.13349-13357. 10.1021/acs.jpcc.2c02404 . hal-03751925

HAL Id: hal-03751925

<https://hal.science/hal-03751925>

Submitted on 16 Aug 2022

HAL is a multi-disciplinary open access archive for the deposit and dissemination of scientific research documents, whether they are published or not. The documents may come from teaching and research institutions in France or abroad, or from public or private research centers.

L'archive ouverte pluridisciplinaire **HAL**, est destinée au dépôt et à la diffusion de documents scientifiques de niveau recherche, publiés ou non, émanant des établissements d'enseignement et de recherche français ou étrangers, des laboratoires publics ou privés.

Physical interactions tune the chemisorption of polar anions on carbon nanostructures

Anwar Hasmy,^{*,†,‡} Luis Rincón,[¶] Adrien Noury,[§] François Henn,[‡] and Vincent Jourdain[‡]

[†]*Departamento de Física, Universidad Simón Bolívar, Valle de Sartenejas, 1080 Caracas, Venezuela*

[‡]*Laboratoire Charles Coulomb, Univ Montpellier, CNRS, 34000 Montpellier, France*

[¶]*Grupo de Química Computacional y Teórica and Instituto de Simulación Computacional, Universidad San Francisco de Quito, Quito 170901, Ecuador*

[§]*Laboratoire Charles Coulomb, Univ Montpellier, CNRS, 34090 Montpellier, France*

E-mail: anwarhasmy@hotmail.com

Abstract

Density functional tight-binding calculations of the adsorption of OH^- and other related diatomic anions on carbon nanotubes and graphene show that two adsorption states coexist: a physisorption state caused by Debye interactions, and a chemisorption state at shorter distances dominated by ionic-covalent interactions. For all anions, both adsorption energies scale linearly with the curvature of the carbon surface, and increase with decreasing anion polarizability but also, in metallic nanotubes, with chiral angle. At short distances, charge transfer modifies the attractive Debye forces into repulsive forces of the dipole-dipole type, tuning the strength of the chemisorption state, and may determine its existence and stability.

1. Introduction

The behavior of carbon nanostructure interfaces in presence of a liquid electrolyte has attracted a lot of interest due to their potential applications in energy and environmental technologies. These notably include supercapacitors for energy storage,¹⁻³ capacitive deionization for water desalination and purification.³⁻⁵ The occurrence of electrical charges at the carbon surface, resulting from specific ion adsorption, is of utmost importance for such applications. In particular, high surface charge densities have been evidenced during the transport of aqueous electrolytes inside carbon nanotubes (CNTs), which was proposed to arise from hydroxide (OH^-) adsorption based on the strong pH dependence.^{6,7} It has also been argued that graphene becomes electrically charged in degassed water due to the spontaneous adsorption of OH^- ions on its surface.⁸ Since ion adsorption can change both the electrical properties of CNTs and the ionic conductivity of the confined electrolyte, a detailed understanding of this adsorption is crucial.

Electronic structure calculation methods constitute a powerful tool to that end. For monoatomic ions such as H^+ , Li^+ , Mg^+ , Mg^{2+} , Be^{2+} , among others, it has been evidenced that the adsorption can be either covalent or non-covalent, depending on the chemical species and charges.⁹⁻¹⁴ For heteronuclear diatomic ions such as OH^- , little is known about the origin and nature of the binding process, especially concerning the potential effect of their dipole moment. For OH^- adsorption on graphene, Density Functional Theory (DFT) calculations in vacuum have shown that the bond length between the oxygen and the nearest carbon is equal to 1.5 Å with a binding energy of 0.5 eV.¹⁵ However, the detailed nature of OH^- adsorption has not been investigated to date, neither in the case of graphene, nor in that of CNTs which are technologically important and where additional curvature effects are expected.

In this work we study the adsorption of OH^- and structurally close anions, such as bisulfide (SH^-) and hypochlorite (ClO^-), on graphene and on the inner and outer surfaces of single-walled CNTs (SWCNTs) in vacuum conditions and by neglecting thermal fluctuations

($T=0$ K), using the Self-Consistent Charge Density Functional based Tight-Binding (SCC-DFTB) method.¹⁶ Our results show that two adsorption states coexist: a physisorption state dominated by Debye interactions between the anion and the carbon surface, and a chemisorption state at shorter distance. Both adsorption energies increase linearly with the surface curvature. However, for metallic CNTs, the higher the chiral angle, the lower the adsorption energies. In contrast to previous works,^{15,17} we show that the OH^- adsorption at short distance results from a polar covalent bond whose strength is tuned by repulsive physical interactions of dipole-dipole type.

2. Methods

The SCC-DFTB method has been widely used for electronic structure calculations of CNTs^{18,19} and their adsorption properties.^{20–22} Here we use the corresponding third-order expansion of the Kohn-Sham total energy in DFT with respect to charge density fluctuations.²³ Nanotube diameters vary from 0.6 to 3 nm, and the smallest nanotube length L_x is 1.71 nm, which corresponds to a variation from 128 to 824 C atoms per unit cell depending on the sample. Periodic boundary conditions (PBC) are used to minimize finite size effects, and the tube length of the pristine samples was chosen by analyzing the convergence of the total density of states (DOS) with sample size (see Figure S1 in the Supporting Information SI). Our study includes calculations on metallic (M) armchair (n, n) , on metallic and semiconducting (SC) zigzag $(n, 0)$ and chiral (n, m) ($n \neq m$) SWCNTs. A graphene sheet of 240 C atoms per unit cell is also included for comparison.

First, the geometry of pristine carbon nanostructures are optimized using the L-BFGS method.²⁴ Next, the anion is placed perpendicular to the tube axis at a given distance d_{SA} from the carbon surface, while the counterion (K^+) is placed in the same direction, but at the greatest possible distance (> 35 Å) to minimize undesired electrostatic effects at the adsorption region (Figure S2a in SI). Finally, the positions of the anion’s atom closest to the

surface (i.e. O for OH⁻ and ClO⁻, and S for SH⁻) and of its nearest C atom (named C₀) are fixed (which is equivalent to fixing a bond length between them), while the other atoms are again fully relaxed using the L-BFGS method.

To assess the most favorable site for OH⁻ adsorption on the carbon surface, we explored binding on different high-symmetry sites, and found that the most favorable situation is the Top-symmetry where the O atom faces the carbon atom C₀ (Figure S2b in SI). In this case, C₀ is the only carbon atom fixed, hence the distance d_{SA} is equivalent to its distance with O. In the following, our calculations thus focus on the Top-symmetry adsorption for all ions.

The energy profiles due to interactions between the anion and the carbon nanostructure can be defined in the illustrative case of OH⁻ by:

$$E(d_{SA}) = E_{tot}(d_{SA}) - E_C - E_{OH-K}(d_{OH-K}), \quad (1)$$

where E_{OH-K} and E_C are the interaction energies for the OH⁻ anion and the counterion K⁺ (separated by a distance d_{OH-K}), and for the pristine carbon nanostructure, respectively. $E_{tot}(d_{SA})$ is the total energy of the system for the anion and the carbon nanostructure at distance d_{SA} . The binding (adsorption) energy E_B is defined as the opposite value of the energy where $E(d_{SA})$ exhibits a minimum: using this convention, the higher the value, the stronger the binding. In addition, atomic Mulliken charges, bond lengths and other quantities that account for the deformation of the carbon surface around the adsorption region are calculated. The projected density of states and the isosurface charge density difference are also evaluated to assess the changes in the electronic structure during the adsorption process.

Finally, to deepen our analysis of the adsorption process, we have performed energy profile calculations by forbidding any carbon surface deformation originating from chemical interactions with the anions. For this, once the pristine carbon nanostructures are relaxed and the anion is located at a distance d_{SA} of the carbon surface, the position of all C atoms

are fixed as for O (or S) and C₀ atoms. Only H (or Cl) atoms are allowed to move during the structure optimization. Furthermore, the energy profiles of OH⁻ adsorption on some CNT samples have been calculated in presence of implicit water, using the Generalized Born Approximation as implemented in the DFTB package,¹⁶ which excludes periodic boundary conditions. Although this kind of approximation neglects any possibility of proton transfer between OH⁻ and water molecules, it is able to model some of the screening effects of liquid water on the anion-CNT system.

3. Results

3.1. Energy profiles

Figures 1a-c show the energy profiles for endo- and exohedral adsorption of OH⁻ on M-armchair, M-zigzag and SC-zigzag SWCNTs, with different diameters. For comparison, the energy profile of graphene is included (thick black line). In the endohedral case (thick solid curves), an energy minimum of -0.25 ± 0.05 eV is observed at $d_{sA} \sim 2.3 \pm 0.3$ Å (Figures S3a,b in SI). Moreover, separated by an energy barrier, another minimum is found at 1.57 ± 0.04 Å: the narrower the tube, the shallower this minimum. It is metastable for small diameters but becomes dominant over that at $2.1 - 2.5$ Å for diameters larger than 3 nm, 1.4 nm and 0.95 nm for M-armchair, SC-zigzag and M-zigzag tubes, respectively.

For exohedral adsorption (thick dashed curves) and for graphene (thick black line), we observe only one energy minimum which is located at $d_{sA} = 1.50 \pm 0.03$ Å and becomes deeper with decreasing tube diameter (Figures S3a,b in SI). In contrast to the endohedral case, no other minimum is visible at larger distance. However, the large width of the energy well supports that it results from the combination of the two minima previously observed. The binding energy (E_{B_1}) varies from 0.54 eV for graphene to 1.34 eV for the smallest CNT diameter (0.95 nm) shown in Figure 1a-c (and even 1.6 eV for a M-zigzag CNT of 0.7 nm diameter, see Figure S3b in SI). For comparable tube diameters, the binding energy

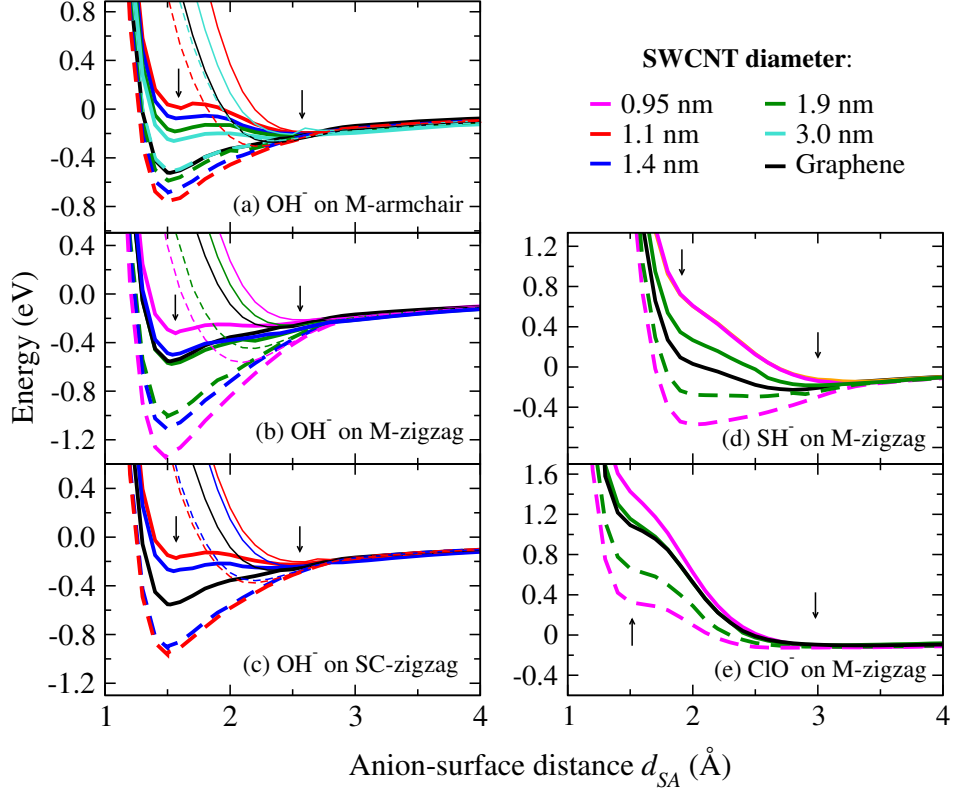


Figure 1: Energy profiles of the OH^- adsorption on (a) M-armchair, (b) M-zigzag, and (c) for SC-zigzag SWCNTs, when the anion is inside (thick solid curves) or outside (thick dashed curves) tubes with different diameters. Results for SH^- and ClO^- on M-zigzag CNTs are shown in (d) and (e), respectively. The graphene case (black curves) is included for comparison. All these profiles correspond to the Top-symmetry adsorption situation. The arrows indicate the two energy minima associated with the two different adsorption states. The thinner curves in (a), (b) and (c) depict the profiles when the protrusion of the binding C_0 atom is forbidden during the optimization process, and the colors and line styles correspond to those used in the thick curves to define the diameter and type of adsorption (exo- or endohedral).

E_{B_1} follows the order: $E_{B_1}(\text{M-zigzag}) > E_{B_1}(\text{SC-zigzag}) > E_{B_1}(\text{M-armchair})$. Note that our results for graphene ($E_{B_1} = 0.5$ eV and $d_{SA} = 1.52$ Å) and our observation of a weaker adsorption inside CNT agree with previous DFT calculations.^{15,17} However, our results evidence the coexistence of two adsorption states and that the binding energy E_{B_1} strongly depends on both the curvature and chirality of the nanotube.

Figs. 1d,e show that for SH^- and ClO^- , the results are qualitatively similar to OH^- : an energy minimum is observed for SH^- and ClO^- at $d_{SA} \sim 3.1$ and 2.5 Å, respectively, with

an additional adsorption state at ~ 2 and 1.5 \AA . However, the states at shorter distances are always unstable, except for SH^- exohedral adsorption (see also Figures S3c,d in SI).

The thinner curves in Figures 1a-c and the curves in Figure S4 in the SI show the energy profiles when the protrusion of the C_0 atom is forbidden (undistorted tube) for all anions and for different diameters and chiralities. As can be seen, in such a situation where chemical interactions are hindered and physical ones thus dominate, the energy minimum at $2 < d_{SA} < 3.2 \text{ \AA}$ is clearly visible, including when no energy barrier separate it from the chemisorption state in the relaxed CNT profiles (i.e. for OH^- exohedral adsorption on CNTs).

3.2. Atomic charges

We now analyze the Mulliken atomic charges for the different atoms involved as a function of the distance d_{SA} in those anions where a stable chemisorption state exists (OH^- and exohedral SH^-). Figs. 2a and 2b show that the negative charges of O and S, respectively, reduce when decreasing d_{SA} from $\sim 3 \text{ \AA}$, while their signs prevail. The charge of the C_0 atom changes from 0 to a positive value and the total charges of its adjacent C_1 atoms become negative. We find that the charge transfer values are similar regardless of the CNT chirality and diameter, and of the adsorption configuration (endo- or exohedral).

In the case of OH^- , charge transfers between the anion and the carbon surface are observed for $d_{SA} \leq 2 \text{ \AA}$ (Figure 2a). The lack of charge transfer for $d_{SA} > 2 \text{ \AA}$ shows that the adsorption state at $2.1 - 2.5 \text{ \AA}$ has no or very little ionic character. In contrast, at $d_{SA} \sim 1.5 \text{ \AA}$, the large and opposite signs of the O and C_0 charges reveal that the corresponding adsorption state possesses a significant attractive ionic component. Indeed, the four atoms at the corner of the tetrahedron (O and three C_1) acquire a negative charge, while the C_0 atom at its center becomes positive, as occurs in polar bonded alcohols.²⁵ Actually, the charge transfer occurs from the anions OH^- and SH^- (in exohedral adsorption), to the carbon surface, and the C_0 , O and S atoms act as charge donors, while the C_1 atoms

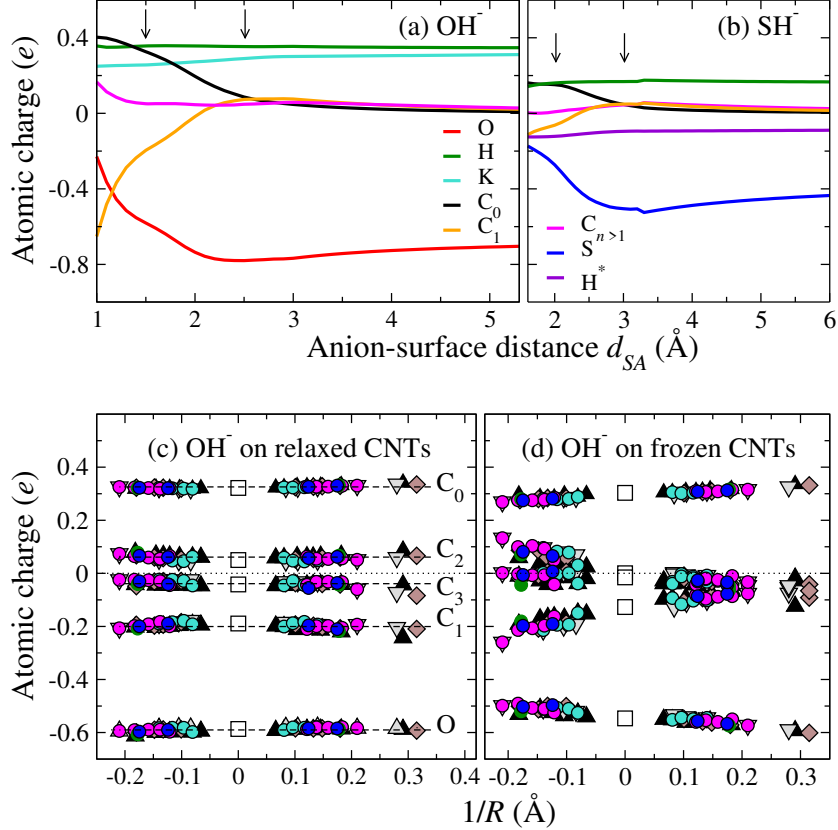


Figure 2: Mulliken atomic charges as a function of the distance d_{SA} for (a) OH^- and (b) SH^- . The arrows denote the d_{SA} distances where the energy minima take place. C_n refers to the charge contributions of the first ($n = 1$), second ($n = 2$) and third ($n = 3$) C atom neighbors of C_0 . Atomic charges as a function of the curvature $1/R$ for OH^- on (c) relaxed and (d) unrelaxed CNTs at $d_{SA} \sim 1.5 \text{ \AA}$. The symbols correspond to M-armchair (black triangles), M-zigzag (grey triangles), SC-zigzag (brown diamonds), SC-chiral (blue circles) and M-chiral (magenta, turquoise and green circles) nanotubes, and graphene (open squares).

act as acceptors, which supports the chemical character of the bond at short equilibrium distances and leads to a change in the tube polarization as will be discussed below. Figures 2c,d depict the atomic charges as a function of the curvature $1/R$ for OH^- adsorbed on (c) relaxed and (d) unrelaxed CNTs at the shorter equilibrium distance ($d_{SA} = 1.5 - 1.6 \text{ \AA}$).

Fig. 2c evidences that regardless of whether the diameter of the tube increases or decreases, whether the adsorption is endo or exohedral, the atomic charges do not change significantly. We have found the same for SH^- . Furthermore, for the adsorption state at $d_{SA} = 1.5-1.6 \text{ \AA}$, the sign of the atomic charges of C_n atoms oscillate in a damped manner as the positions of $\text{C}_{n>0}$ neighbor atoms are further away from C_0 , until they become neutral.

In the case of the adsorption on unrelaxed CNTs at equilibrium distance similar to that of Fig. 2c, we found that a charge transfer also occurs. However, in contrast to the case of relaxed CNTs, a slight curvature dependence is observed for O and C_0 for the adsorption of OH^- (Fig. 2d), while the charge contributions of the $C_{n>0}$ atom neighbors behave differently depending on whether the anion is outside or inside the tube. Note that no dependence on the tube type is observed, as in the relaxed CNT situation. These results show that freezing carbon atoms to hamper chemical interactions do not prevent charge transfers between atoms.

3.3. Density of states

To understand the nature of the O- C_0 bond, we calculate the projected DOS at $d_{SA} = 1.5$ and 2.5 \AA for both endo- and exohedral adsorption. Figure 3 displays the s-states of C_0 , and the p-states of its adjacent C_1 and O atoms for M-armchair (Figures 3a,b,d,e) and M-zigzag (Figures 3c,f) for ~ 1 -nm tube diameters (for SC-zigzag, see Figure S5 in SI). The energy window is chosen to highlight the s- and p-states hybridization, and are plotted with respect to the Fermi energy ($E - E_F$). For endohedral chemisorption ($d_{SA} = 1.5 \text{ \AA}$), the C_0 s-states (black curve) totally overlap with the C_1 p-states (blue curve) (Figures 3b,c), which shows that the sp^2 character of pristine bonded C-C atoms prevails. Besides, the partial overlap between the C_0 s-states and O p-states reveals a low covalence degree in the O- C_0 bonding. Conversely, the larger overlap between C_0 s-states and O p-states for exohedral chemisorption (Figures 3e,f) shows an increase of the O- C_0 bond covalence with respect to the endo case, which occurs at the expense of a lower covalence in C_0 - C_1 bonds at $E - E_F \approx -10 \text{ eV}$. For $d_{SA} = 2.5 \text{ \AA}$ (Figures 3a,b), no hybridization is observed between C_0 s- and O p-states, as expected for physical bonding.

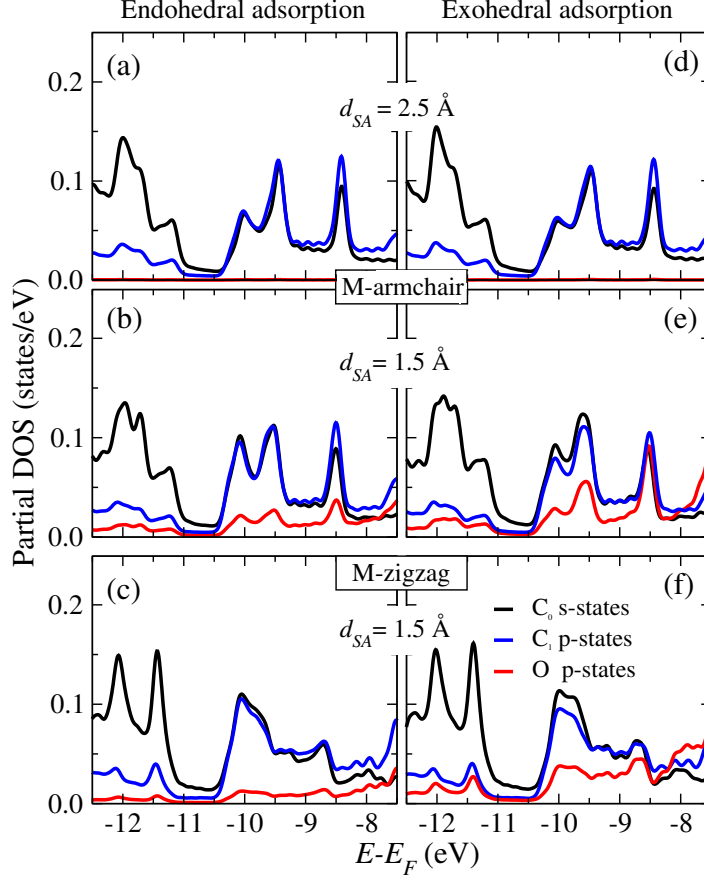


Figure 3: Partial DOS corresponding to s-states of C_0 (black curve), and p-states of its adjacent C_1 (blue curve) and O (red curve) atoms, for OH^- endo- and exohedral adsorption at $d_{SA} = 2.5$ and 1.5 Å, on M-zigzag and armchair CNTs of 1.1 and 0.95-nm diameters, respectively. The energy scale was chosen to highlight the total and/or partial overlaps between the s- and p-states involved in the bonding hybridization.

3.4. Charge density difference

To illustrate the charge redistribution around the adsorption site, Figure 4 depicts the iso-surface charge density difference (total density minus the sum of the atomic densities) for OH^- adsorbed on M-armchair SWCNTs of 1.1-nm diameter at $d_{SA} = 1.5$ and 2.5 Å, and for both cases (endo and exohedral adsorptions). The electron depletion regions are colored in red and the accumulation regions in blue: as an illustration, the blue region surrounding the red one in the oxygen atom (see Fig. 4) is associated to its lone pair, and gives account of the charge transfer between H and O.

At $d_{SA} = 1.5$ Å, the depletion region along the O- C_0 bonding outlines its covalent

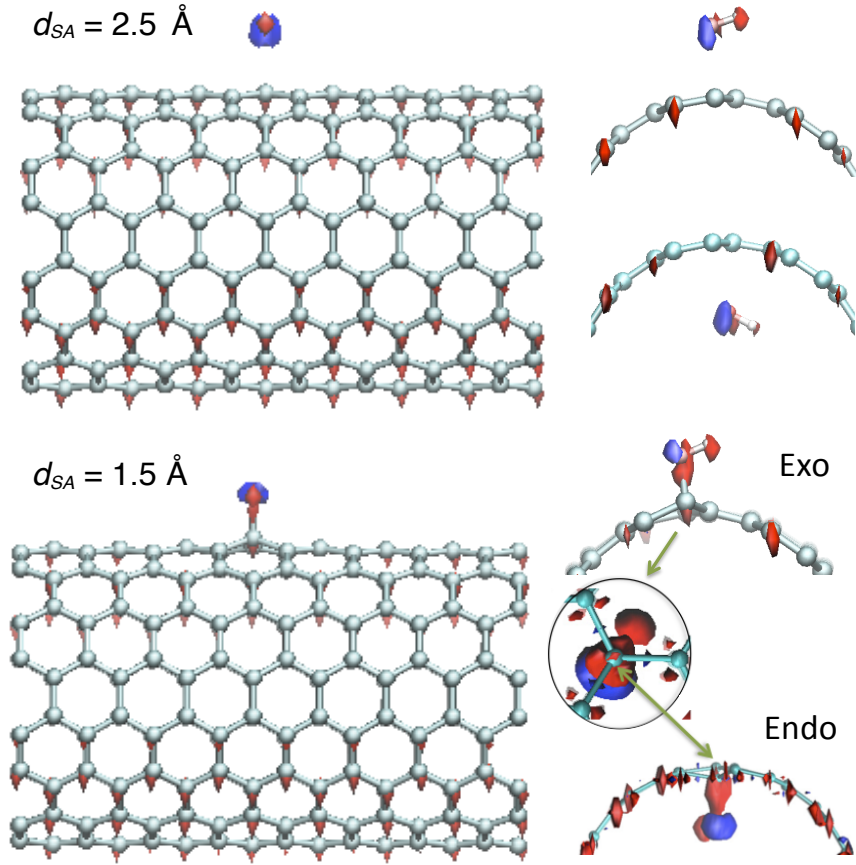


Figure 4: Isosurface charge density difference (total density minus sum of atomic densities) for the adsorption of OH⁻ for M-armchair tube at $d_{SA}=1.5$ and 2.5 \AA at $d_{SA}=1.5 \text{ \AA}$. Red and blue denote the electron depletion and accumulation regions, respectively. The isovalue is equal to $0.05 e/\text{\AA}^3$, except for the M-armchair fragment on the right whose isovalue is equal to $0.025 e/\text{\AA}^3$. The arrows indicate a depleted region that emerges at C₀ but behind the bonding direction with O. The inset magnifies this effect for the endo case to highlight such depleted region outside the tube in C₀ in endo adsorption. These results correspond to calculations on M-armchair SWCNTs of 1.1-nm diameter.

character (Fig. 4 right bottom panel). In contrast, this depletion does not occur at $d_{SA} = 2.5 \text{ \AA}$ (Fig. 4 right top panel), which confirms its physical character. Besides, for exohedral adsorption at $d_{SA} = 1.5 \text{ \AA}$, a depleted region emerges inside the tube at the back of C₀ (see arrows in Fig. 4): this shows that C₀ antibonding states become partially occupied, giving rise to a repulsive contribution to the chemisorption energy. For endohedral adsorption and $d_{SA} = 1.5 \text{ \AA}$, a depletion region also appears but at lower isovalues ($0.02 e/\text{\AA}^3$), which implies a larger occupancy of the anti-bonding states and a lower binding with respect to exohedral adsorption. Additionally, the isosurface charge density plots at

both $d_{SA} = 1.5$ and 2.5 \AA reveal a long-range charge redistribution made of linear patterns of depletion regions aligned along the tube axis in both CNTs (Fig. 4 left panels). As later discussed, these patterns reveal a polarisation of the nanotube originating from physical interactions with OH^- , which supports the existence of dipole-dipole type interactions at both d_{SA} .

3.5. Adsorption energies versus nanotube surface curvature

Figure 5a shows the binding energy E_{B_1} at $d_{SA} = 1.5 \text{ \AA}$ as a function of the curvature $1/R$, for the different anions and carbon nanostructures considered here. Negative curvature values correspond to concave CNT surfaces and positive values to convex ones as conventionally done.²² Negative E_{B_1} values correspond to metastable or unstable states. A linear relationship is observed between E_{B_1} and the tube curvature, in agreement with previous electronic structure calculations on neutral adsorbents. Indeed, it has been shown that E_{B_1} depends linearly on the tube curvature by means of the relation:^{21,22,26-30}

$$E_{B_1} = E_0 \pm A/R, \tag{2}$$

where the positive and negative sign applies for exo- and endohedral adsorption, respectively. The monotonic increase in energy with $1/R$ was attributed to the surface pyramidalization that contributes to a local rehybridization from sp^2 to sp^3 at the adsorption site C_0 , thus favoring chemical interactions in the exohedral case and unfavoring them in the endohedral one.^{31,32} Therefore, the narrower the tube, the higher the pyramidalization at the exohedral adsorption site. Similar arguments explain the opposite effect on concave surfaces.²² Table S1 of the SI provides the E_0 and A values obtained from linear regressions, which evidences that the slope A does not change significantly in our case, yielding for OH^- a slope $A = 2.3 \pm 0.2 \text{ eV\AA}$ regardless of the tube type (Figure 5a), while E_0 clearly depends on the tube chirality. For neutral adsorbates, previous energy decomposition analysis (EDA) has shown

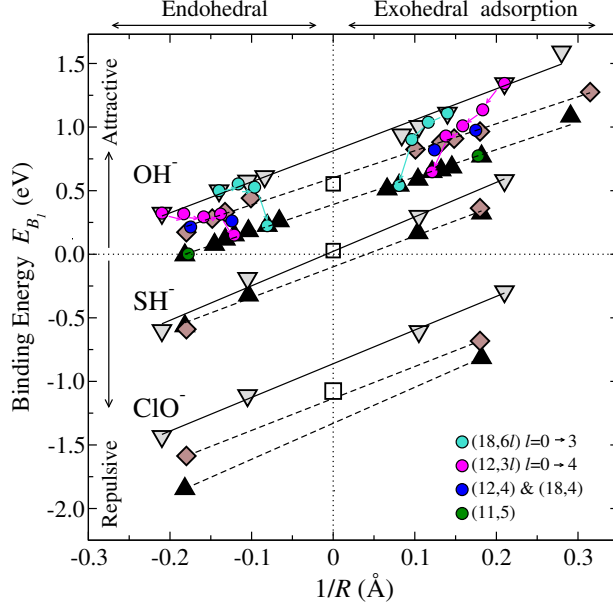


Figure 5: Binding energy E_{B_1} of different anions as a function of the tube curvature (inverse radius $1/R$) for different tube types.

that for chemisorption, E_{B_1} is dominated by a $1/R$ term derived from the adsorbate-surface interaction.^{21,22} The quadratic contribution that characterizes the strain energy associated to the tube curvature ($2.14/R^2$ eVÅ²^{33,34}) is small compared to linear contributions, and according to EDA there are other terms that cancel each other out.

Previous DFT studies on neutral radical adsorbates have shown that $A = 3.14$ eVÅ for H and Al adsorbed on M- and SC-zigzag CNTs,²⁶ 2.5 eVÅ for NH₂ on M-armchair,²⁷ and 3.2 and 4.3 eVÅ for OH, COOH and F on SC-zigzag and M-CNTs (armchair and zigag), respectively.²⁸ It is also reported that E_0 in Eq. (2) (i.e. E_{B_1} extrapolated to $1/R = 0$) matches the adsorption energy on graphene.^{21,26,27,29} This agrees with our results for OH⁻ on SC-CNTs, but not for M-zigzag and M-armchair CNTs where E_0 is, respectively, 0.2 eV lower and higher than on graphene. We also studied M-chiral CNTs: as shown in Figure 5a for (12,3*l*) and (18,6*l*) tubes, E_{B_1} decreases with increasing chiral angle. At the opposite, SC-chiral CNTs such as (12,4) and (18,4) display values similar to those of SC-zigzag. These results show that, beside curvature-induced rehybridization, chiral angle-dependent effects also impact E_{B_1} in the case of M-CNTs.

For SH^- and ClO^- , the results are qualitatively similar to OH^- : for both anions E_{B_1} behaves linearly with the curvature $1/R$ with a slope A slightly larger than that of OH^- ($A = 2.6$ and $2.8 \text{ eV}\text{\AA}$ for SH^- and OCl^- , respectively). For a given CNT, E_{B_1} follows the order: $E_{B_1}(\text{OH}^-) > E_{B_1}(\text{SH}^-) > E_{B_1}(\text{ClO}^-)$ (Figure 5a). Interestingly, this order correlates with the inverse of the anion polarizability (see Table S2 in SI).

3.6. Carbon surface pyramidalization

As mentioned above, when an anion is chemisorbed on the carbon surface, the C_0 atom protrudes due to the local rehybridization from sp^2 to sp^3 that takes place around the adsorption region (see Fig. 4). Such protrusion has already been observed in previous DFT studies of OH^- adsorbed on graphene¹⁵ and SWCNTs.¹⁷ Indeed, the analysis of the carbon surface deformation can inform about the nature of the adsorption process.^{9,29,32} The protrusion height h can be defined as the shortest distance between the C_0 atom and the plane made by its three adjacent C_1 atoms, that is $h = a_{\text{C}_0\text{C}_1} \sin \theta_p$, where θ_p ($=\theta_{\sigma\pi} - 90^\circ$) denotes the pyramidalization angle and $\theta_{\sigma\pi}$ is the average bond angle $\langle \text{O-C}_0\text{-C}_1 \rangle$ ⁹ (see Fig. 6a). For OH^- chemisorbed on SWCNTs with different diameters, Fig. 6b plots θ_p as a function of the distance d_{SA} . The scale on the right side corresponds to the protrusion height h , and solid and dashed lines to endo- and exohedral adsorption, respectively. For $d_{SA} \geq 3 \text{ \AA}$, the sign of θ_p is positive for exohedral adsorption and negative for endohedral adsorption. This implies that the tube curvature contributes to a variation of θ_p from $\pm 1.7^\circ$ to $\pm 5.7^\circ$ for the largest (2.4-nm) and narrowest (0.7-nm) tubes, respectively. A small deviation of $\pm 1^\circ$ is found for graphene which we attribute to weak long-range electrostatic interactions resulting from the presence of OH^- . For $d_{SA} < 3 \text{ \AA}$ the angle θ_p increases as d_{SA} decreases, until the equilibrium distance of the chemisorption state is reached (see arrows in Fig. 6b). For $2 < d_{SA} < 3 \text{ \AA}$, the θ_p angle ranges from -5° to 6° due to the tube curvature, for the narrower CNTs in the endo- and exohedral situations, respectively. This agrees with a physisorption state at $d_{SA} \sim 2.4 \text{ \AA}$ since the sp^2 character of the pristine carbon nanostructures is preserved.

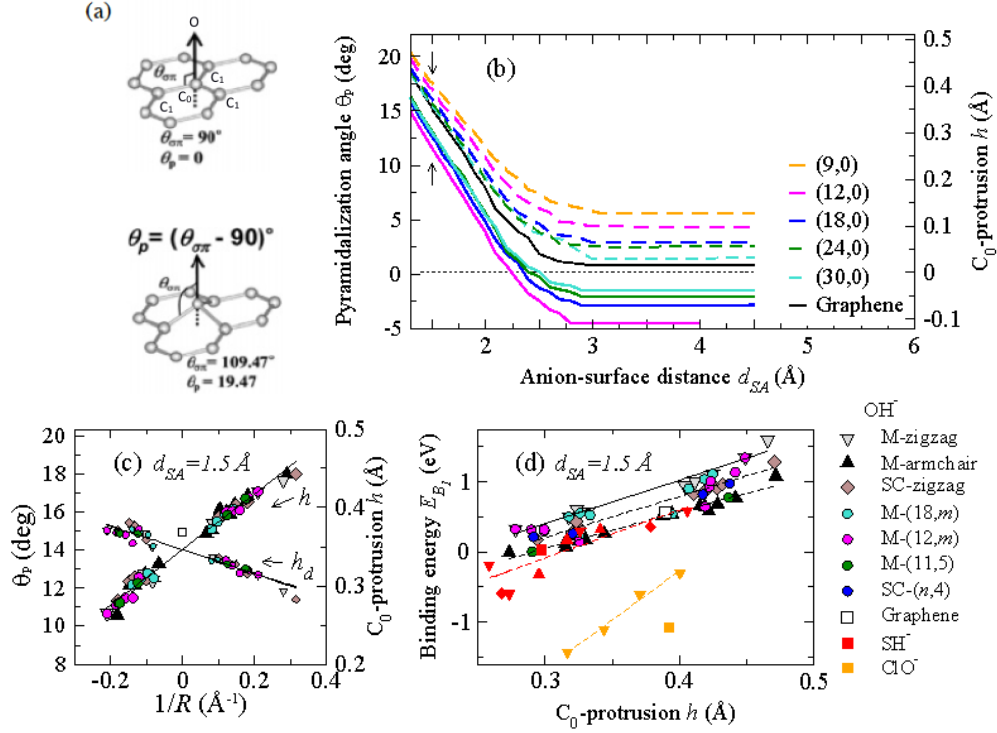


Figure 6: (a) Illustration of the pyramidalization angle θ_p at the adsorption site, and (b) the pyramidalization angle θ_p (the scale at the right side associates to the protrusion height h) versus the distance d_{SA} for OH^- endo (solid lines) and exohedral (dashed lines) adsorption on tubes of different diameters. The graphene case is included for comparison. (c) Plot of θ_p and h (and h_d , small symbols) as a function of the tube curvature ($1/R$) at $d_{SA} \sim 1.5 \text{ \AA}$, and (d) Binding energy E_{B_1} versus the protrusion height h of the C_0 atom for all anions. Red and orange symbols correspond to SH^- and ClO^- , respectively. The solid and dashed lines are linear regressions on the different M- and SC-tube curves.

For $d_{SA} \sim 1.5 \text{ \AA}$, Fig. 6c shows that the θ_p (and h) scales linearly with the tube curvature $1/R$ from 10.5° to 17.5° , corresponding to endo- and exohedral chemisorption of OH^- on the narrowest tube, respectively. For graphene the value is 15° . Then, the larger the angle θ_p (and the height h), the larger is the degree of hybridization, as it approaches the angle of a perfect tetrahedron. In contrast, the $\langle C_{1i}-C_0-C_{1j} \rangle$ angle decreases from 120° for pristine CNTs to $111 - 117^\circ$ when the anion is chemisorbed. These results lead to a slight decrease in the C_0 -O bond length a_{C_0O} with increasing curvature, and the smaller this bond becomes the larger the C_0 - C_1 bond length $a_{C_0C_1}$ (see Fig. S6 in SI). In Fig. 6c the solid line corresponds to a linear regression, which yielded $\theta_p = 0.245 \pm 0.255/R$ (in rad). Additionally, the

protrusion height h scales linearly from 0.27 to 0.48 Å with $1/R$, and a linear regression yielded $h \sim 0.37 \pm 0.39/R$ (Å). These trends are reminiscent of the difference between purely sp^2 bonded graphene and sp^3 carbon structure. For purely sp^3 bonded diamond the equivalent quantity to h is 0.51 Å, $a_{CC} = 1.54$ Å and $\langle C-C-C \rangle = 109.5^\circ$.

We also estimate the protrusion height h_d , originating from the covalent interaction with the anion, without the contribution of the tube curvature. For this we take into account that $h = h_i + h_d$, where h_i is the height associated to the curvature of pristine CNTs. We checked that $h_i = \pm a_{C_0C_1}^2/4R \sim \pm 0.51/R$ (Å) with $a_{C_0C_1} = 1.43$ Å. The sign of h_i opposes the sign of the curvature-dependent term of h_d due to the underlying pyramidalization of the tube surface which plays in favor or against protrusion formation, depending on whether the adsorption is exo- or endohedral. Hence, for a given anion, a linear regression yielded $h_d = E_h \mp A_d/R$ (Å), with $E_h = 0.37$ and $A_d=0.12$ (see Fig. 6c, smaller symbols). In addition, Fig. 6d plots the binding energy E_{B_1} as a function of h . The solid and dashed lines correspond to linear regressions of OH^- on M-armchair, M-zigzag and SC-zigzag, which gives $-1.53+5.25h$, $-1.45+6.20h$, and $-1.55+5.85h$, respectively. For the other anions on M-zigzag CNTs, we found $-12.15+6.88h$ for SH^- and $-5.90 + 14.08h$ for ClO^- .

4. Discussion

To unravel the origin of the differences in E_{B_1} between different tube types, we implement an energy decomposition analysis based on the evaluation of the protrusion of C_0 atom. Since $h = E_h \pm A_h/R$ regardless the tube type (E_h and A_h are constants), combined with Eq. (2) leads to:

$$E_{B_1}(h) = E_0 - A_r E_h + A_r h \quad (3)$$

where $A_r = A/A_h$. Figure 6d confirms that Eq. (3) fits well our data.

In absence of protrusion (i.e. $h = 0$) our data reveals that the negative term in the sum of Eq. (3) dominates, which unveils a repulsive non-covalent energy contribution. In addition,

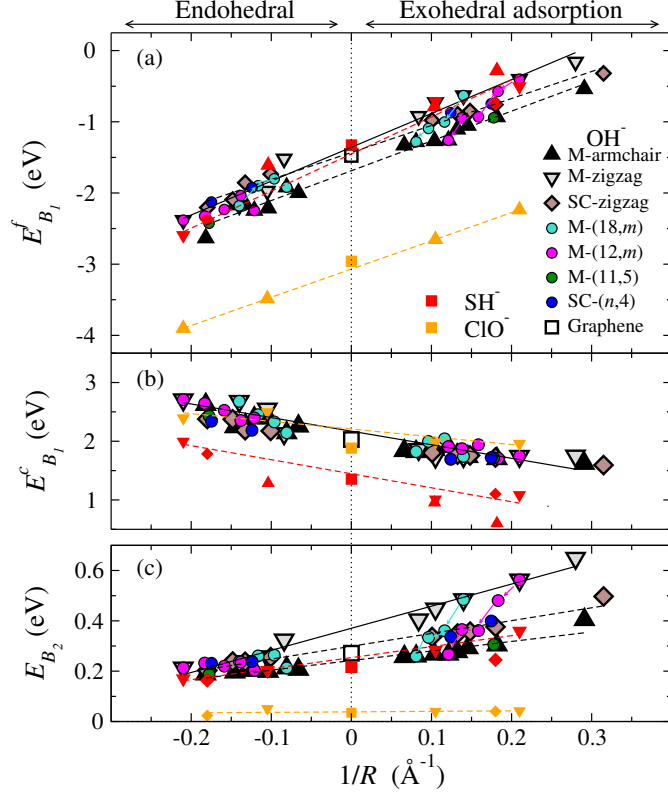


Figure 7: (a) Energy $E_{B_1}^f$ on frozen CNTs, and (b) $E_{B_1}^C (= E_{B_1} - E_{B_1}^f)$ at $d_{SA} \sim 1.5 \text{ \AA}$, and (c) the binding energy $E_{B_2} (= E_{B_2}^f)$ at $d_{SA} \sim 2.4 \text{ \AA}$, as a function of $1/R$ for different anions. Solid and dashed lines in (a) and (c) correspond to linear regressions, and in (b) to the covalent energy due to the surface deformation $E_{B_1}^C$ found for chemisorbed anions on relaxed CNTs (see the text).

since $h = h_i + h_d$, we can decompose E_{B_1} according to the nature of the surface deformation. Thus, from Eq. (3) one can infer that the covalent energy contribution due to the surface deformation h_d is $E_{B_1}^C = A_r h_d$. Note that this term dominates over that originating from h_i (i.e. the contribution of the tube curvature at most deviates the h value by $\pm 30 \%$ for the narrower tubes with respect to that of graphene, see Figure 6c). In terms of $1/R$ it leads to $E_{B_1}^C \simeq E_h A/A_h \mp (A_d/A_h)(1/R)$. Since $E_{B_1}^C$ does not depend on E_0 , one can conclude that the differences in chemisorption energy between tube types must originate from non-covalent interactions.

We validate the above energy decomposition analysis from the computed energy profiles when the positions of all C atoms being frozen to prevent the protrusion formation. This

suppresses the corresponding sp^3 covalent interactions, but non those originating from the tube curvature. As shown above, the resulting profiles in Figure 1 (thin curves) and in Figure S4 in SI, evidence attractive contributions at intermediate distances (2.1 – 2.5 Å). At 1.5 Å the energy minima are suppressed, but charge transfers and their distributions around the chemisorption region remain almost similar to those of relaxed tubes (Figure 2c and 2d): this shows that the attractive ionic contribution is preserved in frozen CNTs. Figure 7a shows that the energy $E_{B_1}^f$ at $d_{sA} \sim 1.5$ Å is repulsive (negative) and scales linearly with $1/R$ for all anions. Figure 7b plots the energy difference $E_{B_1} - E_{B_1}^f$ as a function of $1/R$ (symbols) to show that it behaves similar to the linear expression found for $E_{B_1}^C(1/R)$ (solid and dashed lines). This implies that the ionic and physical contributions in frozen and relaxed tubes are equivalent, which proves the robustness of our approach. It also confirms that at $d_{sA} \sim 1.5$ Å, a repulsive contribution originates from non-covalent interactions in relaxed tubes. Moreover, for OH^- , linear regressions yielded $E_{B_1}^f = -1.69 + 4.2/R$, $-1.43 \pm 3.8/R$ and $-1.36 \pm 4.75/R$ (eV) for M-armchair, SC-zigzag and M-zigzag, respectively. Since the atomic charges are similar in both cases, and these contributions show the same trends as E_0 depending on the tube-type, one may conclude that the E_{B_1} differences are caused by physical interactions.

For SH^- (red symbols), although the energy $E_{B_1}^f$ behaves similarly to that of OH^- , $E_{B_1}^C$ does not: this means that the weaker chemisorption of SH^- originates mostly from its weaker ionic-covalent bonding with carbon, as confirmed by its smaller charge transfer (see Figure 2) and smaller orbital hybridization (see Figure S5 in SI). The opposite is observed for ClO^- (orange symbols), which means that the chemisorbed state is unstable because repulsive non-covalent interactions are too strong. Interestingly, the similarity between the non-covalent energy contributions of OH^- and SH^- , and their differences with ClO^- , correlates with the order of the dipole moments of the isolated anions (see Table S2 in SI).

For $d_{sA} > 2$ Å, the energy minima provide a good estimate for the binding energy E_{B_2} corresponding to the physisorbed state of relaxed CNTs since there is no charge transfer.

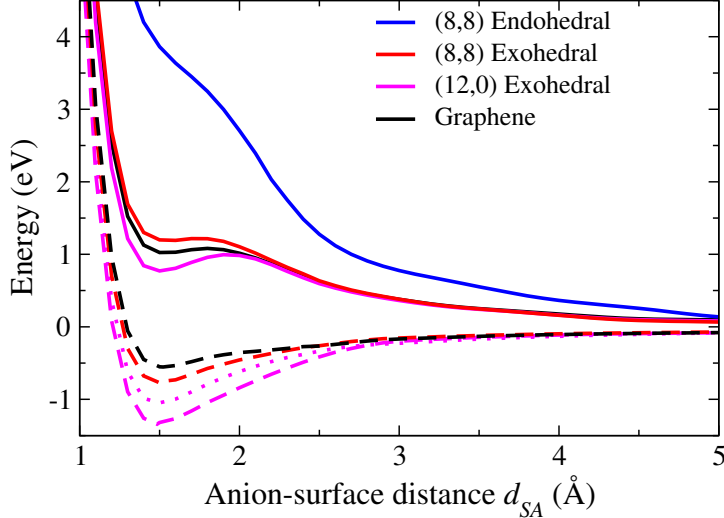


Figure 8: Energy versus the distance d_{SA} of OH^- adsorbed on graphene, M-armchair and M-zigzag tubes with small diameters, with implicit water ($\epsilon = 80.2$), solid lines) and in vacuum conditions (dotted lines). In both cases the tube length is ~ 2 -nm and periodic boundary conditions (PBC) are neglected. For comparison, dashed lines show some of the energy profiles depicted in Fig. 1 which include PBC.

Figure 7c shows that its attractive character increases linearly with the curvature of M-armchair, M-zigzag and SC-zigzag CNTs, but with a slope which is at least three times smaller than for chemisorption (Table S1 in SI). Interestingly, the resulting binding energies at $d_{SA} \sim 1.5$ (Figure 7a) and ~ 2.4 Å (Figure 7c) follow similar trends with the tube type as E_{B_1} versus $1/R$ in Figure 5a, which supports that the energy differences between tube types come from non-covalent interactions.

We now discuss the nature of the long-range attractive physical interactions which cause physisorption at $2.1 - 2.5$ Å and modulate chemisorption at 1.5 Å. The fact that *i*) non-polar ions such as H^+ and K^+ do not display this physisorbed state (see Figures S3e,f in SI) and that *ii*) CNTs display long-range polarization patterns in the isosurface charge density difference strongly supports the hypothesis of Debye interactions. This is additionally validated by calculations of the CNT dipole moments. Here, the dipole moments μ_z along the $\text{O}-\text{C}_\text{O}$ bond axis and μ_{xy} in the xy -plane (perpendicular to the bond axis) were estimated separately due to the symmetry of the system. Figs. S7a,b in SI show that for $d_{SA} < 3$ Å, μ_{xy} of CNTs increases with decreasing d_{SA} from 3 Å, while for OH^- it reaches a maximum at $d_{SA} \sim 2.5$ Å.

The opposite occurs for μ_z , i.e., it reaches a maximum for CNTs at that distance, while for the OH^- it disappears for $d_{SA} < 3 \text{ \AA}$. The latter suggests that the orientation of the OH^- dipole moment changes from being perpendicular to the xy -plane to being parallel. Indeed, μ_z dominates over μ_{xy} in the physisorption state, while the opposite occurs in the chemisorption state, which can be associated to the charge transfer that occurs for $d_{SA} < 2 \text{ \AA}$: The dipole moment of the CNT becomes permanent and changes its orientation. As a consequence the OH^- dipole moment also changes, and although the attractive chemical interactions between the CNT and the anion dominate, the respective dipole moments tend to acquire the same orientation, generating a source of dipole-dipole repulsion (Figure S7 in SI). Furthermore, the dipole moments scale with nanotube radius as R^2 up to $d_{SA} = 2.5$ and 1.5 \AA in agreement with previous work,³⁵⁻³⁷ while we find that the slope depends slightly on the type of tube.

Finally, Fig. 8 shows the resulting energy profiles (solid lines) of OH^- with selected carbon nanostructures in presence of implicit water. The curves are compared to the profiles calculated in vacuum conditions with PBC (dashed lines) and without PBC (dotted lines). The results evidence that for M-armchair tube the adsorption is unstable (i.e. the barrier energy is smaller than 0.1 eV) and it is metastable for exohedral adsorption on M-(12,0) CNT. Fig. 8 also shows the results for graphene, although in this case it is to be expected that finite size effects do not exhibit the same tendencies as CNTs due to symmetry differences.

5. Conclusions

In conclusion, for polar anions on carbon nanostructures, we showed that a physisorption state caused by Debye interactions coexist with a chemisorption state at shorter distances dominated by ionic-covalent interactions. Importantly, the physical dipole-dipole interactions strongly tune the chemisorption energy at smaller distance and govern the effective stability of the chemisorption state. Having demonstrated the key role of physical interactions at the fundamental level, a key question is now the influence of the solvent on these interactions.

Our preliminary calculations on finite-length CNTs with implicit water ($\epsilon = 80.2$) suggest that the screening effects impact the stability of the chemisorption state, in agreement with previous DFT calculations of OH^- on graphene with implicit¹⁵ and explicit³⁸ water. However, for exohedral adsorption on CNTs, we find that the chemisorption state may shift from stable to metastable or even unstable depending on the carbon nanostructure (see Figure 8). In the case of OH^- adsorption inside carbon nanotubes and graphene nanoslits, the strong decrease of dielectric constant experimentally observed for confined water may reduce the screening of dipole-dipole and ionic interactions and preserve the chemisorption (meta)stability.³⁹ Owing the complexity of water interactions, more simulations using explicit water would be needed to address these questions.

Acknowledgements

We thank E. Anglaret and A. Penicaud for fruitful discussions, and the BioNano-NMRI team (L2C, UM) for computer facilities. We acknowledge the support of the Agence Nationale de la Recherche (France) through the IONESCO project (ANR-18-CE09-0011-01) and from CNRS-MITI (France) through a 'Momentum' grant. A.H. acknowledges support from the CNRS (France).

Supporting Information

The Supporting Information includes: Computational details, energy profiles, Mulliken atomic charges, Density of States, Isosurface charge density difference, bond lengths, pyramidalization angles, dipole moments, and OH^- adsorption with implicit water, figures and tables.

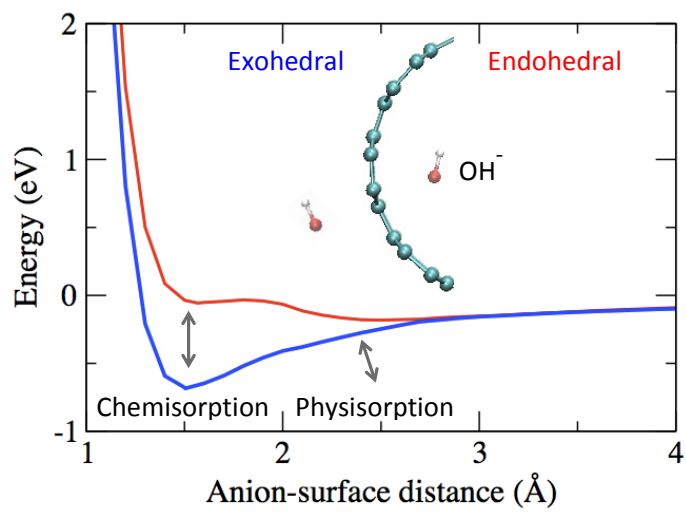
References

- (1) Simon, P.; Gogotsi, Y. Materials for electrochemical capacitors. *Nat. Mater.* **2008**, *7*, 845–854.
- (2) Siria, A. M.; Bocquet, M. L.; Bocquet, L. New avenues for the large-scale harvesting of blue energy. *Nat. Rev. Chem.* **2017**, *1*, 0091.
- (3) Pakulski, D.; Czepa, W.; Del Buffa, S.; Ciesielski, A.; Samori, P. Atom-thick membranes for water purification and blue energy harvesting. *Adv. Funct. Mater.* **2019**, 1902394.
- (4) Porada, S.; Zhao, R.; Van Der Wal, A.; Presser, V.; Biesheuvel, P. Review on the science and technology of water desalination by capacitive deionization. *Prog. Mater. Sci.* **2013**, *58*, 1388–1442.
- (5) Zhang, C.; He, D.; Ma, J.; Tang, W.; Waite, T. D. Faradaic reactions in capacitive deionization (CDI)-problems and possibilities: a review. *Water Res.* **2018**, *128*, 314–330.
- (6) Secchi, E.; Niguès, A.; Jubin, L.; Siria, A.; Bocquet, L. Scaling behavior for ionic transport and its fluctuations in individual carbon nanotubes. *Phys. Rev. Lett.* **2016**, *116*, 154501.
- (7) Yazda, K.; Tahir, S.; Michel, T.; Loubet, B.; Manghi, M.; Bentin, J.; Picaud, F.; Palmieri, J.; Henn, F.; Jourdain, V. Voltage-activated transport of ions through single-walled carbon nanotubes. *Nanoscale* **2017**, *9*, 11976.
- (8) Bepete, G.; Anglaret, E.; Ortolani, L.; Morandi, V.; Huang, K.; Pénicaud, A.; Drummond, C. Surfactant-free single-layer graphene in water. *Nat. Chem.* **2017**, *9*, 347–352.
- (9) Ruffieux, P.; Gröning, O.; Biemann, M.; Mauron, P.; Schlapbach, L.; Gröning, P. Hydrogen adsorption on sp^2 -bonded carbon: Influence of the local curvature. *Phys. Rev. B* **2002**, *66*, 245416.

- (10) Liu, Z. H⁺ ions on graphene electrode as hydrogen storage reservoirs. *Comput. Mater. Sci.* **2011**, 50, 3257–3264.
- (11) Umadevi D.; Sastry, G. N. Metal ion binding with carbon nanotubes and graphene: Effect of chirality and curvature *Chem. Phys. Lett.* **2012**, 549, 39–43.
- (12) Colherinhas, G.; Fileti, E. E.; Chaban, V. V. The band gap of Graphene is efficiently tuned by monovalent ions. *J. Phys. Chem. Lett.* **2015**, 6, 302–307.
- (13) Zhu, C.; Yang, G. Insights from the adsorption of halide Ions on graphene materials. *ChemPhysChem* **2016**, 17, 2482–2488.
- (14) Aslanzadeh, S. A. A computational study on the potential application of zigzag carbon nanotubes in Mg-ion batteries. *Struct. Chem.* **2020**, 31, 10731–1078.
- (15) Grosjean, B.; Pean, C.; Siria, A.; Bocquet, L.; Vuilleumier, R.; Bocquet, M. Chemisorption of hydroxide on 2d materials from DFT calculations: graphene versus hexagonal boron nitride. *J. Phys. Chem. Lett.* **2016**, 7 (22), 4695–4700.
- (16) Aradi, B.; Hourahine, B.; Frauenheim, T. DFTB+, a sparse matrix-based implementation of the DFTB method. *J. Phys. Chem. A* **2007**, 111, 5678–5684.
- (17) Mejri, A; Herlem, G.; Picaud, F.. From Behavior of Water on Hydrophobic Graphene Surfaces to Ultra-Confinement of Water in Carbon Nanotubes. *Nanomaterials* **2021**, 11, 306.
- (18) Peralta-Inga, Z.; Boyd, S.; Murray J. S.; O Connor, C. J.; Politzer, P. Density Functional Tight-Binding studies of carbon nanotube Structures. *Struct. Chem.* **2003**, 14, 431–443.
- (19) Rincón, L.; Almeida, R.; González, C. A. On the charge carrier localization in zigzag carbon nanotube junctions. *J. Phys. Chem. C* **2011**, 115, 11727–11733.

- (20) Seo, K.; Park, K. A.; Kim, C.; Han, S.; Kim, B.; Lee, Y. H. Chirality- and diameter-dependent reactivity of NO₂ on carbon nanotube walls. *J. Am. Chem. Soc.* **2005**, *127*, 15724–15729.
- (21) Zheng, G.; Wang, Z.; Irle, S.; Morokuma, K. Origin of the linear relationship between CH₂/NH/O-SWNT reaction energies and sidewall curvature: armchair nanotubes. *J. Am. Chem. Soc.* **2006**, *128*, 15117–15126.
- (22) Wang, Z.; Irle, S.; Zheng, G.; Morokuma, K. Analysis of the relationship between reaction energies of electrophilic SWNT additions and sidewall curvature: chiral nanotubes. *J. Phys. Chem. C* **2008**, *112*, 12697–12705.
- (23) Gaus, M.; Goez, A.; Elstner, M. Parametrization and benchmark of DFTB3 for Organic Molecules. *J. Chem. Theory Comput.* **2013**, *9*, 1, 338–354.
- (24) Nocedal, J.; Wright, S. J. "Numerical optimization" (Springer, NY, 2nd ed, 2006).
- (25) NIST Computational Chemistry Comparison and Benchmark Database, <http://cccbdb.nist.gov> (2020).
- (26) Gülseren, O.; Yildirim, T.; Ciraci, S. Tunable adsorption on carbon nanotubes. *Phys. Rev. Lett.* **2001**, *87*, 116802.
- (27) Zhao, M.; Xia, Y.; Lewis, J. P.; Mei, L. Chemical reactivity of single-walled carbon nanotubes to amidogen from density functional calculations. *J. Phys. Chem. B* **2004**, *108*, 9599–9603.
- (28) Park, H.; Zhao, J.; Lu, J. P. Distinct properties of single-wall carbon nanotubes with monovalent sidewall additions. *Nanotechnology* **2005**, *16*, 635–638.
- (29) Dam, H. C.; Cuong, N. T.; Sugiyama, A.; Ozaki, T.; Fujiwara, A.; Mitani, T.; Okada, S.. Substrate-mediated interactions of Pt atoms adsorbed on single-wall carbon nanotubes: Density functional calculations. *Phys. Rev. B* **2009**, *79*, 115426.

- (30) Fusaro, M. Derivation of the linear relationship between SWCNTs functionalization energies and sidewall curvature. *Struct. Chem.* **2012**, *23*, 1301–1308.
- (31) Niyogi, S.; Hamon, M. A.; Hu, H.; Zhao, B.; Bhowmik, P.; Sen, R.; Itkis, M. E.; Haddon, R. C. Chemistry of single-walled carbon nanotubes. *Acc. Chem. Res.* **2002**, *35*, 1105–1113.
- (32) Chen, Z.; Thiel, W.; Hirsch, A. Reactivity of the Convex and Concave Surfaces of Single-Walled Carbon Nanotubes (SWCNTs) towards addition reactions: Dependence on the carbon-atom Pyramidalization. *Chemphyschem* **2003**, *1*, 93–97.
- (33) Sánchez-Portal, D.; Artacho, E.; Soler, J. M.; Rubio, A.; Ordejón, P. Ab initio structural, elastic, and vibrational properties of carbon nanotubes. *Phys. Rev. B* **1999**, *59*, 12678–12688.
- (34) Gülseren, O.; Yildirim, T.; Ciraci, S. Systematic ab initio study of curvature effects in carbon nanotubes. *Phys. Rev. B* **65**, 153405 (2002).
- (35) Brothers, E. N.; Kudin, K. N.; Scuseria, G. E. Transverse polarizabilities of carbon nanotubes: A Hartree-Fock and density functional study. *Phys. Rev. B* **2005**, *72*, 033402.
- (36) Novikov, D. S.; Levitov, L. S. Energy Anomaly and Polarizability of Carbon Nanotubes. *Phys. Rev. Lett.* **2006**, *96*, 036402.
- (37) Kozinsky, B.; Marzari, N. Static dielectric properties of carbon nanotubes from first principles. *Phys. Rev. Lett.* **2006**, *96*, 166801.
- (38) Grosjean, B.; Bocquet, M.; Vuilleumier, R. Versatile electrification of two-dimensional nanomaterials in water. *Nat. Commun.* **2019**, *10*, 1656–1661.
- (39) Fumagalli, L.; Esfandiar, A.; Fabregas, R.; Hu, S.; Ares, P.; Janardanan, A.; Yang, Q.; Radha, B.; Taniguchi, T.; Watanabe, W.; Gomila, G.; Novoselov, K. S.; Geimet, A. K. Anomalously low dielectric constant of confined water. *Science* **2018**, *360*, 1339–1342.



TOC graphic